ADVANCED PHYSICS RESEARCH Open Access
www.advphysicsres.com

Unveiling Electron-Phonon and Electron-Magnon Interactions in the Weak Itinerant Ferromagnet $LaCo_2P_2$

*D. Yu. Usachov, K. Ali, G. Poelchen, M. Mende, S. Schulz, M. Peters, K. Bokai, I. Yu. Sklyadneva, V. Stolyarov, E. V. Chulkov, K. Kliemt, S. Paischer, P. A. Buczek, R. Heid, F. Hempel, M. Ruesing, A. Ernst, C. Krellner, S. V. Eremeev, and D. V. Vyalikh**

Studying and understanding many-body interactions, particularly electron-boson interactions, is essential for a deeper elucidation of fundamental physical phenomena and the development of novel material functionalities. Here, this aspect is explored in the weak itinerant ferromagnet $LaCo_2P_2$ by means of momentum-resolved photoelectron spectroscopy (ARPES) and first-principles calculations. The detailed ARPES patterns enable to unveil bulk and surface bands, spin splittings due to Rashba and exchange interactions, as well as the evolution of bands with temperature, which altogether creates a solid foundation for theoretical studies. The latter has allowed to establish the impact of electron-boson interactions on the electronic structure, that are reflected in its strong renormalization driven by electron-magnon interaction and the emergence of distinctive kinks of surface and bulk electron bands due to significant electron-phonon coupling. Our results highlight the distinct impact of electron-boson interactions on the electronic structure, particularly on the itinerant *d* states. Similar electronic states are observed in the isostructural iron pnictides, where electron-boson interactions play a crucial role in the emergence of superconductivity. It is believed that further studies of material systems involving both magnetically active *d*- and *f*-sublattices will reveal more advanced phenomena in the bulk and at distinct surfaces, driven by a combination of factors including Rashba and Kondo effects, exchange magnetism, and electron-boson interactions.

1. Introduction

For over 60 years, lanthanide (Ln) compounds have attracted significant attention due to their rich and unusual properties, including complex magnetic phases, valence fluctuations, heavy-fermion and Kondo behavior, non-Fermi-liquid properties, and unconventional superconductivity (SC).[1–3] The key role here is played by the interaction of itinerant electrons with strongly localized 4*f* shell electrons, which retain their magnetic moments in crystalline solids due to their strong spatial localization. In certain Ln-based intermetallic compounds, transition metal elements may also exhibit magnetic moments. This can result in the coexistence and mutual interactions between strongly localized 4*f* moments and itinerant 3*d* moments, giving rise to the emergence of complex phases, properties, and phenomena.[4–7]

In this regard, it is intriguing to explore and examine the so-called Ln cobalt pnictides family, particularly the $LnCo_2P_2$ series, where both cobalt and Ln

D. Y. Usachov, K. Bokai, E. V. Chulkov
St. Petersburg State University
7/9 Universitetskaya nab., St. Petersburg 199034, Russia
D. Y. Usachov, V. Stolyarov
Moscow Institute of Physics and Technology
Institute Lane 9, Dolgoprudny 141701, Russia
D. Y. Usachov, V. Stolyarov
National University of Science and Technology MISIS
Moscow 119049, Russia

K. Ali
Department of Microtechnology and Nanoscience
Chalmers University of Technology
Göteborg 41258, Sweden
G. Poelchen, M. Mende, S. Schulz
Institut für Festkörper- und Materialphysik
Technische Universität Dresden
Dresden 01069, Germany
M. Peters, K. Kliemt, C. Krellner
Kristall- und Materiallabor, Physikalisches Institut
Goethe-Universität Frankfurt
Max-von-Laue Straße 1, Frankfurt am Main 60438, Germany
I. Y. Sklyadneva, E. V. Chulkov, D. V. Vyalikh
Donostia International Physics Center (DIPC)
Donostia-San Sebastián 20018, Spain
E-mail: denis.vyalikh@dipc.org

The ORCID identification number(s) for the author(s) of this article can be found under https://doi.org/10.1002/apxr.202400137

DOI: 10.1002/apxr.202400137

atoms exhibit magnetic moments in certain materials. The exceptions here are the antiferromagnets $EuCo_2P_2$, where Eu is divalent and Co remains non-magnetic,[8] and $CeCo_2P_2$, where Ce behaves tetravalently in the bulk but demonstrates peculiar magnetic properties near the surface.[9] The competition between the Co–Co, Ln–Co, and Ln–Ln exchange interactions can lead to complex magnetic structures far from being fully understood.

It is worth noting that the family of $LnCo_2P_2$ systems, whose structural and magnetic properties were extensively investigated in 1980–1990s primarily by the W. Jeitschko group, has recently regained strong attention due to the efforts of the M. Shatruk group.[4,5,8] In fact, the $LnCo_2P_2$ systems exhibit a rich spectrum of intriguing bosonic fluctuations. For example, in our recent study of the aforementioned room-temperature metallic antiferromagnet $CeCo_2P_2$, we discovered that this material demonstrates unusual, long-lived magnons even in the terahertz regime.[10] Obviously, the emergence, coexistence, and coupling of bosons such as magnons and phonons with electrons further complicates their mutual interactions.

E. V. Chulkov
Departamento de Polímeros y Materiales Avanzados: Física Química y Tecnología, Facultad de Ciencias Químicas
Universidad del País Vasco UPV/EHU
San Sebastián/Donostia 20080, Spain

E. V. Chulkov
Centro de Física de Materiales (CFM-MPC)
Centro Mixto CSIC-UPV/EHU
San Sebastián/Donostia 20018, Spain

S. Paischer, A. Ernst
Institute for Theoretical Physics
Johannes Kepler University
Altenbergerstr. 69, Linz 4040, Austria

P. A. Buczek
Department of Engineering and Computer Sciences
Hamburg University of Applied Sciences
Berliner Tor 7, Hamburg D-20099, Germany

R. Heid
Karlsruher Institute for Quantum Materials and Technologies (IQMT)
Karlsruhe D-76021, Germany

F. Hempel
Institut für Angewandte Physik
Technische Universität Dresden
Dresden 01187, Germany

M. Ruesing
Paderborn University
Institute for Photonic Quantum Systems (PhoQS)
Warburger Str. 100, Paderborn 33098, Germany

M. Ruesing
Paderborn University
Integrated Quantum Optics
Warburger Str. 100, Paderborn 33098, Germany

A. Ernst
Max-Planck-Institut für Mikrostrukturphysik
Weinberg 2, Halle (Saale) 06120, Germany

S. V. Eremeev
Institute of Strength Physics and Materials Science
Russian Academy of Sciences
Tomsk 634055, Russia

D. V. Vyalikh
IKERBASQUE
Basque Foundation for Science
Bilbao 48011, Spain

It is known that the magnetic properties in $LnCo_2P_2$ systems critically depend on the distance between the Co_2P_2 blocks which are separated by the Ln ions. For example, the aforementioned $EuCo_2P_2$ serves as an illustrative example, where due to the much larger size of Eu^{2+} ions with respect to trivalent Ln ions in other family members, the magnetism on the Co sublattice is completely suppressed. However, by applying pressure, one can significantly influence the P–P distance and, consequently, the oxidation state of Eu.[8] In $LnCo_2P_2$ materials, where Ln represents Ce, Pr, Nd, and Sm, the Co moments exhibit antiferromagnetic (AFM) ordering very close to room temperature.[11] This makes these systems, and particularly their P-Co-P terminated surfaces, attractive for temperature-controlled magnetic switching of magnetically active overlayers. The aforementioned discussion also suggests that $LnCo_2P_2$ systems hold promise for manipulating their magnetic properties through the applica'tion of pressure, and potentially, uniaxial strain.

When discussing the $LnCo_2P_2$ pnictide family, it is noteworthy to mention the remarkable Fe-based 122-type pnictides as well. These compounds exhibit superconductivity up to 38 K, as discovered in 2008.[12] Despite intensive studies, many issues, including the fundamental question about the mechanism of superconductivity, remain open.[13] Moreover, neighboring Ni-based pnictides like $BaNi_2P_2$[14] and $BaNi_2As_2$[15] have also been observed to reveal superconductivity while commensurate/incommensurate charge density wave transition in $BaNi_2(As_{1-x}P_x)_2$ was observed.[16] Additionally, the substitution of $3d$ elements Co and Fe with their respective $4d$ counterparts induces superconducting behavior in $LaRu_2P_2$,[17] $LaRu_2As_2$,[18] and $BaRh_2P_2$.[19] Within these systems, it is suggested that superconducting behavior arises via phonon mediation.

The discussed above systems, apparently, demonstrate a variety of intriguing electron-boson interactions, leading to either superconducting ground states (GS) mediated by spin fluctuations or phonons,[13] or to different magnetic GS, as it is shown schematically in **Figure 1**a. Revealing these competing interactions is crucial for both elucidating fundamental physical phenomena and developing novel material functionalities.

The most direct approach to experimentally explore and address the microscopic properties of such material systems is angle-resolved photoemission spectroscopy (ARPES), which is a surface-sensitive method.[23] This implies that the surface-related properties need to be accurately addressed and separated from bulk phenomena.[9] Note that the magnetic properties at surfaces can significantly differ from those in the bulk due to the emergence of surface states and resonances,[24–26] which open new pathways for exchange interactions as well as coupling to bosonic modes.[27] Potential relaxation and reconstruction processes[28] at the surfaces may further complicate the exploration of the related phenomena from ARPES measurements.

Considering the complexity of the aforementioned electron-boson interactions, which may involve phonons and magnons, as well as surface-related magnetic phenomena, we suggest initiating a comprehensive investigation, beginning with $LaCo_2P_2$. There are several points that make this material unique among the other representatives of the $LnCo_2P_2$ family and curious for the proposed studies (see the magnetic phase diagram of $LnCo_2P_2$ (Figure S1) in the Supporting Information). In particular, it can be considered as the simplest system in the $LnCo_2P_2$

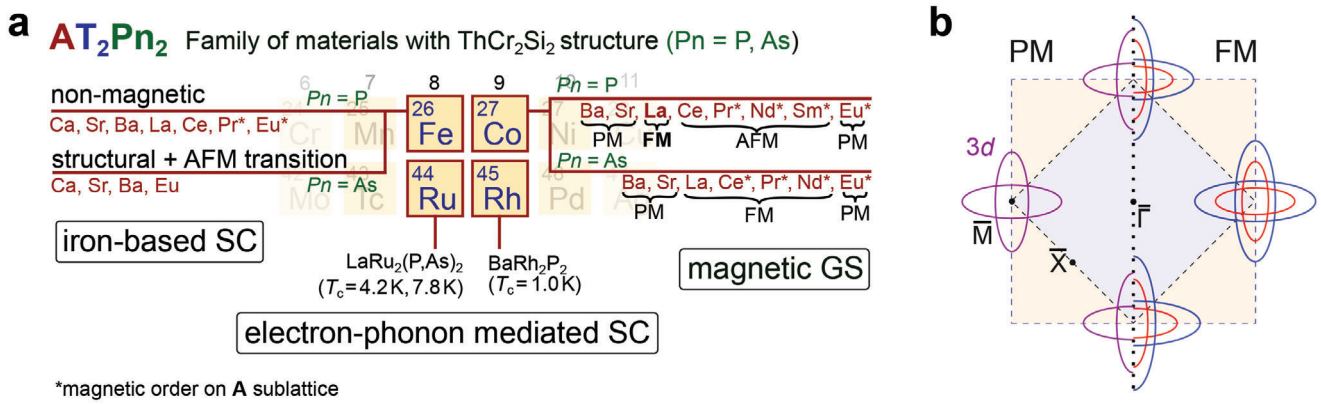

Figure 1. a) Diagram representation of the 122-type transition-metal pnictides and their distinctive properties.[4,11,17–22] b) Sketch of the 3*d* electron pockets at the corner of the Brillouin zone (BZ) for the 122-type transition-metal pnictides[13] in the paramagnetic (PM) and ferromagnetic (FM) phases. In the FM phase, the spin degeneracy is lifted in a majority (blue) and minority (red) band. The larger 1-transition-metal BZ is shown in light orange.

family due to the absence of 4*f* electrons. Next, $LaCo_2P_2$ appears to be on the edge of a magnetic instability, given that the neighboring $BaCo_2P_2$ shows no magnetic order, while the other members of the $LnCo_2P_2$ family do. Furthermore, only $LaCo_2P_2$ exhibits ferromagnetic (FM) ordering of Co 3*d* moments, while other members of the $LnCo_2P_2$ family, where Ln = Ce, Pr, Nd, and Sm, demonstrate AFM ordering in both the Ln and Co sublattices.[4] The latter property is explained by a structural feature of $LaCo_2P_2$, specifically the larger separation between the (Co_2P_2) blocks in comparison to the other members of this family.[4] Additionally, the magnetic order in $LaCo_2P_2$ is highly tunable by doping and structural manipulation through pressure. The reason why the mentioned FM order is essential: it causes spin splitting in otherwise spin-degenerate bands, enabling detailed studies of spin-polarized bands that emerge near the Fermi level and their evolution with temperature. Particularly, this is relevant for the 3*d* electron pockets at the corners of the Brillouin zone (BZ) (shown in Figure 1b). These pockets are essential for Fermi-surface nesting in the Fe pnictides and are typically located very close to the Fermi level. The lifting of the spin degeneracy, as shown in Figure 1b, shifts the majority states to lower energies, enabling a detailed evaluation of electron-boson interactions.

The high-quality ARPES data presented here allow us to clearly identify bulk and surface electron bands, explore their temperature-dependent evolution, and provide a solid foundation for theoretical studies. Our analysis reveals a complex pattern of interactions, including Rashba effects, magnetic exchange and electron-boson interactions. The most essential findings entail the disentangling and description of electron-phonon and electron-magnon interactions and their distinct impact on the electronic structure of $LaCo_2P_2$. It will be shown that the electron-magnon interaction causes a substantial renormalization of the Co 3*d* derived bands around the $\overline{M}$ point, while the electron-phonon coupling influences the shape of these bands and the emergence of kinks, which vary significantly between surface and bulk bands. Since both magnons and phonons couple to the same electronic state, a strong interplay between both excitations can be assumed.

This is supported by the intriguing observation that the P-terminated surface of $LaCo_2P_2$ remains non-magnetic down to very low temperatures, despite the bulk becoming ferromagnetically ordered below 135 K. Mutual interactions between electrons, phonons, and magnons are likely responsible for the unusual properties observed at the surface. These results thus open avenue for further studies of electron-boson and boson-boson interactions not only in the bulk but also in systems with reduced dimensionality. This is crucial for developing novel multilayers and sequences with unique properties and functionalities.

Finally, on the basis of the ARPES results, we realized a systematic theoretical approach to study systems with strong electron-boson interactions. We considered both electron-magnon and electron-phonon couplings from first principles, combined with an analysis of experimental data. The presented methodology will be valuable for further investigations of related phenomena in many strongly correlated electron systems, beyond just the notable family of 122 transition metal pnictides.

2. Results

$LaCo_2P_2$ is a ferromagnet (FM) with T_C = 135 K[29] which crystallizes in the tetragonal $ThCr_2Si_2$ structure with lattice parameters a = 3.815 Å and c = 11.04 Å.[5,11] Its crystal structure is shown in **Figure 2**a. The cleavage of the $LaCo_2P_2$ single crystal occurs along the plane perpendicular to the crystallographic *c* axis, revealing two distinct surface terminations: a P–Co–P block (P-surface) and La termination.[9] We will primarily focus on the P-terminated surface, whose typical topography is revealed in Figure 2b through scanning tunneling microscopy (STM) measurements performed at a temperature of 4.3 K. STM data show the expected square arrangement of the surface P atoms.[9]

We proceed with the characterization of the electronic structure of the P-terminated crystal in the FM phase through ARPES measurements and density functional theory (DFT) calculations. Our previous DFT studies were performed using a GGA+*U* functional (where GGA stands for generalized gradient approximation) with an effective Hubbard parameter $U_{eff} = U - J = 3$ eV for localized Co 3*d* states.[10] This choice was made to achieve a good agreement with the experimental determination of the Curie temperature and spin waves. The GGA functional delivers the Curie temperature T_C = 52 K, while our choice of the

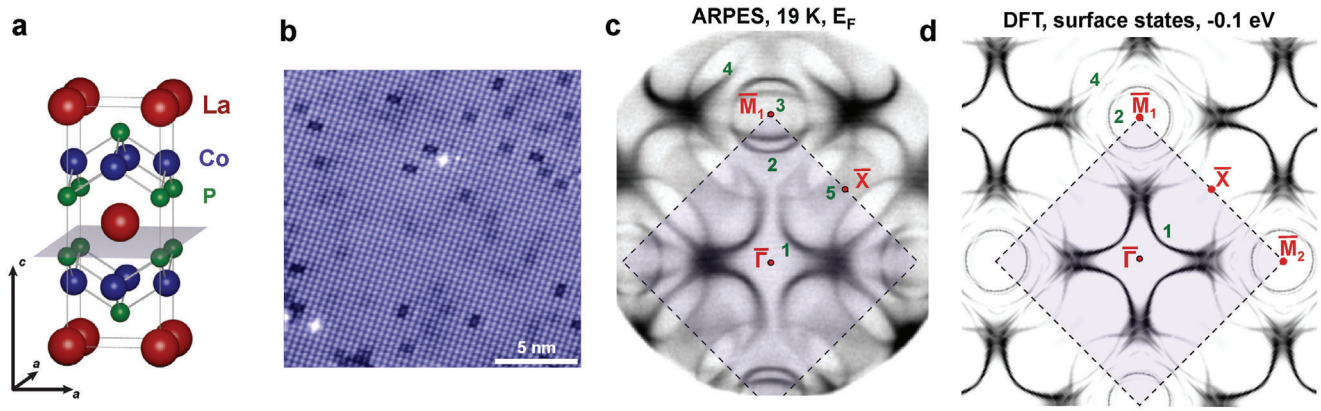

Figure 2. The crystal and electronic structures, along with the STM visualization of the P-terminated surface of $LaCo_2P_2$. a) Tetragonal crystal structure of $LaCo_2P_2$, with the possible cleavage plane between P and La layers highlighted in gray. b) STM image illustrating the topography of the P-terminated surface of a cleaved $LaCo_2P_2$ sample, taken at 4.3 K. c) Fermi surface map obtained through ARPES measurements from the P-terminated surface of $LaCo_2P_2$. A dashed square indicates the surface Brillouin zone. d) Calculated iso-energy map of the surface electronic structure at 0.1 eV below E_F. Darker color corresponds to higher localization of states in the four topmost atomic layers.

GGA+U functional provides $T_C = 130$ K within a random phase approximation. However, magnetic moments of Co, calculated within the GGA+U approximation, are significantly larger than in experiment (0.61 μ_B vs. 0.44 μ_B[30]), while a conventional local spin-density approximation (LSDA) functional delivers a Co moment of 0.48 μ_B. All of these facts indicate the presence of strong spin fluctuations, which can suppress magnetic moments in itinerant magnets.[31] Therefore, we decided to empirically choose the DFT functional, exploring various DFT approximations to achieve the best agreement for the electronic structure derived from our ARPES experiment. Below, we will consider a potential band structure renormalization resulting from electron-boson interactions.

The first and essential step is to unveil surface-related states and distinguish them from bulk states. In Figure 2c,d, we present the ARPES-derived Fermi surface acquired at 19 K and the iso-energy surface obtained using LSDA, respectively. In Figure 2d, we illustrate the calculated constant-energy map of electronic surface states for the P-terminated surface, where the bulk-related states are omitted for simplicity and ease of analysis. To achieve a good agreement between the ARPES-derived Fermi surface and the computed one, we adjusted the latter by a shift of −0.1 eV. This minor discrepancy is attributed to the inherent limitations of DFT accuracy. Upon close inspection, it is evident that the features labeled as 1, 2, and 4 in the computed map are well resolved in the ARPES-derived spectral pattern. These features can be readily identified as surface states intrinsic to the P termination. The band 3 seen in ARPES has a bulk-like origin, it can be derived from a similar calculation performed for the bulk crystal, as illustrated in Figure S4 (Supporting Information).

We continue the analysis of the electronic structure with the results shown in **Figure 3** and begin with band 5, which is distinguishable in the ARPES map at the periphery of the bulk-projected states (Figure 2c), forming the outermost $\bar{M}$-centered contours. One can observe it more clearly on the iso-energy surface taken 0.25 eV below E_F, as depicted in Figure 3(a), where band 5 exhibits a distinct split at 19 K. It is seen that as the temperature increases from 19 to 150 K, the splitting of band 5, highlighted as a pale red spot, diminishes. This is a clear indication that the splitting is primarily associated with the magnetic order. Investigating band 5 further, we found that its $k_{\|}$ splitting is anisotropic with respect to the change in direction from [100] to [$\bar{1}$00]. The difference in splitting is also seen in the $E(k_{\|})$ spectrum (Figure 3(b)) where two different values of splitting, marked as Δ_1 (~60 meV) and Δ_2 (~130 meV), are observed. The revealed asymmetry in the splitting originates from two fundamental phenomena: the Rashba spin-orbit (SO) coupling and magnetic exchange interaction.[32–35] Itinerant electrons near the surface are influenced by the effective magnetic fields arising from these interactions. As a result, in momentum space this is reflected through the discernible asymmetry in the spin splitting of the surface electron band. In the considered case, on one side of the $\bar{X}$ (or $\bar{M}$) point, the effective SO field aligns with the exchange field (or magnetization **M**), whereas on the opposite side they manifest opposite orientations, thereby giving rise to the aforementioned asymmetry in the splitting.[32–35]

Figure 3f displays the constant energy contour calculated at −0.35 eV for the nonmagnetic state of $LaCo_2P_2$, revealing the spin polarization of surface-related states near the corner of the surface BZ (S_y component is shown). The typical spin structure of the Rashba spin-split surface states, especially for state 5, can be easily seen. Thus, our results indicate the emergence of the Rashba effect along with the presence of in-plane magnetization at the P-termination.[32–35] From the observed asymmetry, it is possible to determine the magnetization direction, as illustrated by the blue arrow in Figure 3a. Note that the sample was not magnetized before the measurements. Consequently, the surface is expected to have differently oriented magnetic domains. The acquisition of ARPES data from only one domain suggests that the domains are significantly larger than the size of the photon beam,[33] which was approximately 15 μm in diameter. It is essential to note that no Rashba effect is possible in the bulk centrosymmetric crystal of $LaCo_2P_2$. Therefore, it is the additional confirmation that band 5 is localized near the surface. Our calculations reveal that band 5 exhibits surface resonance properties with pronounced localization within the topmost two P–Co–P

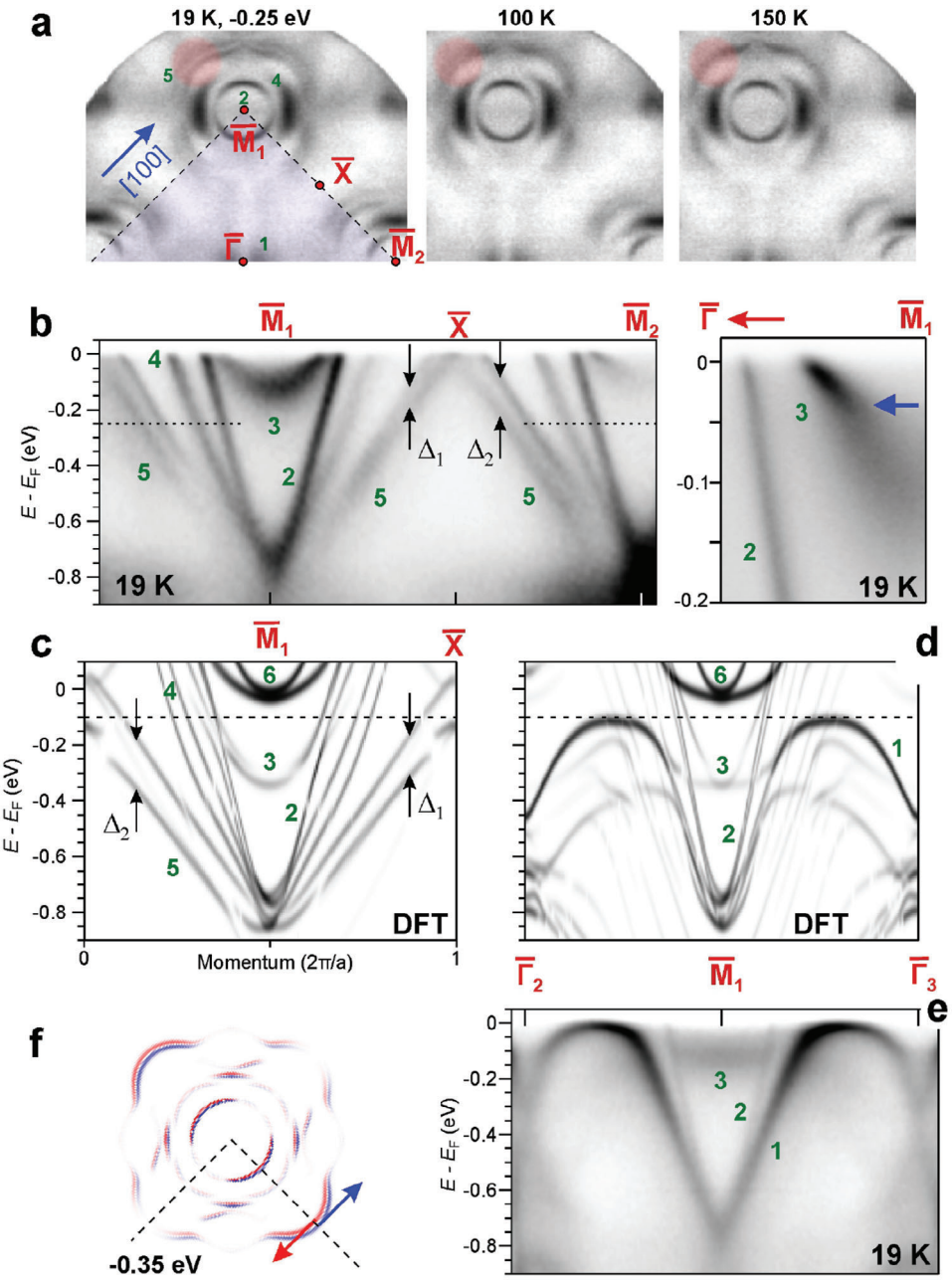

Figure 3. Electronic structure of the P-terminated surface of $LaCo_2P_2$. a) ARPES-derived iso-energy maps at 0.25 eV below E_F illustrate the temperature-dependent evolution of band *5*, highlighted by a pale red spot. The blue arrow denotes sample the magnetization along [100]. b) Cut along the $\bar{M}_1 - \bar{X} - \bar{M}_2$ direction of the surface Brillouin Zone, as marked in Figure 2d, acquired with ARPES at 19 K. c) Theoretical surface band structure in the same direction as in (b); Darker color corresponds to higher localization of states in the six topmost atomic layers. d) Results of the same calculation plotted along the $\bar{\Gamma}_2 - \bar{M}_1 - \bar{\Gamma}_3$ direction, and e) the corresponding ARPES data. f) Calculated constant-energy map of surface states (localized in the four top layers) in the paramagnetic phase, with colors indicating the spin polarization along the [100] direction.

trilayers. The calculations also highlight an asymmetric splitting of band 5 which is seen in Figure 3c, supporting our interpretation.

The DFT results also indicate that Co in the topmost P-Co-P block is nonmagnetic, and the surface-related exchange magnetism originates from the Co in the next block (sixth layer below the P-termination). We evaluated the SO splitting of band 5 in the calculated spectrum at the distance of ±0.3 reciprocal lattice units (r.l.u.) from the $\bar{M}$ point, as $|\Delta_2 - \Delta_1|/2 = 23$ meV and the exchange splitting as $|\Delta_2 + \Delta_1|/2 = 0.15$ eV.

From the ARPES derived Δ_1 and Δ_2 we obtained the SO splitting of ~0.03 eV and the exchange splitting of ~0.09 eV (at 19 K). As one can see the experimental exchange splitting is essentially smaller than the calculated one. This may indicate that magnetization even in the second cobalt layer, that is the sixth atomic layer below the P-termination, is noticeably

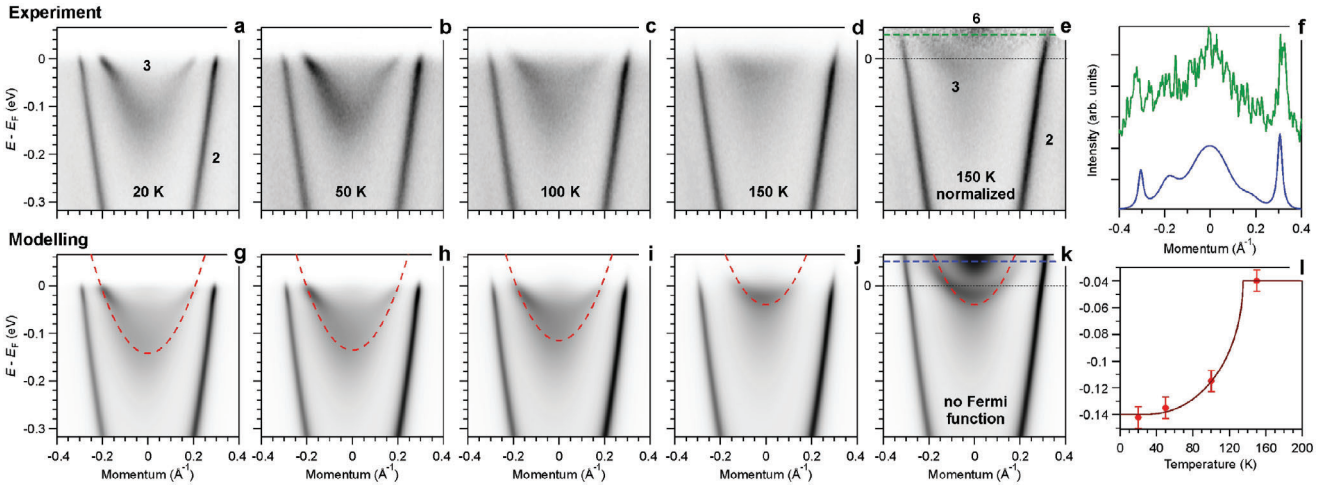

Figure 4. The ARPES-derived temperature evolution of band 3 near the $\bar{M}$ point taken along the $\bar{\Gamma} - \bar{M} - \bar{\Gamma}$ direction (a–e) and its simulation using the parabolic band dispersion and model self-energy (g–k). In (e) the intensity was normalized to its average value for each energy, while in (k) the intensity was not multiplied by the Fermi function. f) Profiles of the measured and simulated PE intensity at 50 meV above the E_F. l) Temperature-dependent changes in the energy position of the bottom of band 3 without renormalization (corresponds to the red dashed lines in (g–k) that show the bare band).

smaller than that in the bulk. As we will see further this statement is in agreement with the analysis of the properties of band 3.

Let us discuss the previously mentioned surface band 1, well-visible in Figure 3d,e. It does not display the spin splitting anticipated for a ferromagnetic P–Co–P surface block. Our DFT calculations suggest that this splitting is absent and therefore remains undetected in ARPES due to the negligible magnetic moment and the absence of magnetic order in the first Co layer beneath the P-terminated surface. Summarizing our current observations, we conclude that in the atomic layers below the P-terminated surface of $LaCo_2P_2$, Co exhibits distinctly different magnetic moments as compared to the bulk. Specifically, the first Co layer behaves non-magnetically, while the second Co layer (sixth atomic layer) below the P-surface displays non-zero moments and undergoes magnetic ordering, resulting in the exchange splitting of band 5.

Our calculations show that the magnetic moment of Co in the second atomic layer is highly sensitive to the distances between neighboring layers. According to calculations, alteration in the P–Co distance by a few percent can result in substantial variations in the magnetic moment, even including the possibility of its sign reversal. The mentioned variations in P–Co distance are comparable to the amplitudes of atomic zero vibrational modes. Therefore, it is plausible that phonons exert a strong influence on the electronic subsystem, potentially leading to significant modifications in surface-related magnetic properties. In this regard, it is essential to note that the ARPES data highlight a significant kink in band 3 near the E_F. This can be seen in the right panel of Figure 3b, where the mentioned kink is indicated by a blue arrow.

This observation may be attributed to electron-boson interaction, specifically pointing towards electron-phonon and/or electron-magnon coupling. It is important to note that our recent resonant inelastic X-ray scattering (RIXS) measurements on $LaCo_2P_2$ indicate the presence of magnons at the similar energy range.[10] Our next point of discussion will revolve around this particular subject, and namely electron-boson interaction in the bulk and at the surface of $LaCo_2P_2$.

In **Figure 4**, we illustrate the temperature evolution of the spectral pattern, including bands 2 and 3 near the $\bar{M}$ point, obtained from ARPES experiment and modeling. As mentioned earlier, DFT calculations indicate that the sharp band 2 represents a surface state intrinsic to the P-terminated crystal. Essentially, it shows no significant changes with temperature, consistent with the absence of magnetization at the surface. Note that our additional experiment, involving Rb deposition onto the freshly-cleaved P-surface (not shown), demonstrates a charge transfer from Rb, affecting the energy position of the surface state 2, while band 3 remains unaffected that confirms its bulk nature. The ARPES experiment depicted in Figure 4a–d reveals a gradual shift of band 3 towards E_F with increasing temperature. This observation suggests that band 3 represents a spin-polarized state due to exchange splitting. In accordance with our DFT calculations, this band is occupied by Co 3*d* majority spin electrons. Additionally, it implies the existence of a counterpart of band 3 with the opposite spin, positioned above the E_F. In fact, such state can be observed in the bulk band structure of $LaCo_2P_2$ projected along the [001] direction shown in Figure S4 (Supporting Information). With increase of temperature both bands are shifted towards the Fermi level reducing herewith the exchange splitting. Above the Curie temperature (paramagnetic state, simulated within the disordered local moment (DLM) method,[36] Figure S7b, Supporting Information), the bands are degenerate in the vicinity of the M point and are broadened due to a strong spin disorder. It is noteworthy that DFT calculations uncover the presence of band 6 just above the E_F seen in Figure 3c,d. While it has a similar origin to band 3, band 6 is distinct. It is localized near the non-magnetic P-surface and, as a result, does not show exchange splitting. Indeed, the bottom of this surface band 6 can be seen in Figure 4e, where we show the ARPES intensity taken at 150 K and normalized by its momentum-integrated value. More clearly it is illustrated in Figure 4f, where one can observe a broad peak with its maximum at the $\bar{M}$ point in the momentum distribution

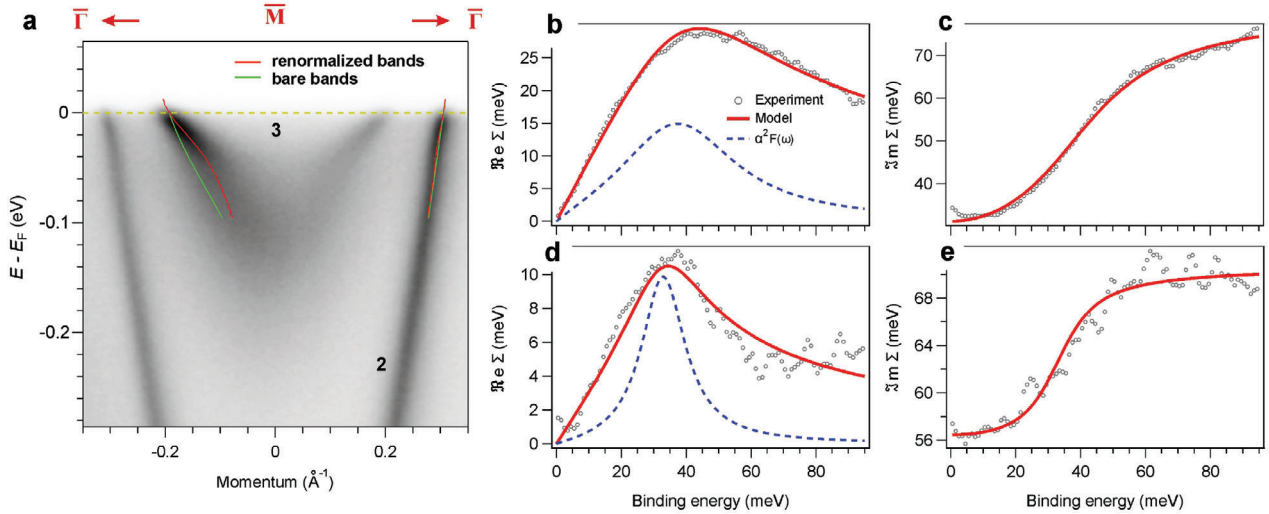

Figure 5. Analysis of electron-phonon coupling for the bands 2 and 3. a) ARPES data taken along the $\bar{M} - \bar{\Gamma}$ direction of the surface BZ. Real (b) and imaginary (c) parts of the self-energy $\Sigma(E)$ for the band 3. d,e) The same for the band 2. Dashed lines demonstrate the model Eliashberg function.

curve (MDC) shown in green, taken at 50 meV above the E_F. The blue line shows the result of modeling (Figure 4k) which we discuss further.

The spin-polarized band 3 exhibits a pronounced renormalization and kink-like behavior in close proximity to the E_F, suggesting substantial many-body interactions in $LaCo_2P_2$. The latter complicates the precise determination of the energy shift of band 3 as a function of temperature. To address this issue, we present simulated ARPES data in Figure 4g–k for careful evaluation of the experimental data. In our modeling, we used parabolic band dispersions with manually adjusted curvature and intensity. As next, we applied renormalization to bands 2 and 3 using the self-energy derived from ARPES, as will be discussed in detail below. The dashed parabola shows the unperturbed (bare) band 3. Its position as a function of temperature is given in Figure 4l. The solid line here indicates a magnetization of a spin-1/2 system derived from the mean-field model. The good agreement between the modeled line and the determined positions of band 3 confirms that the shift is attributed to exchange splitting. However, the magnitude of the splitting is only 0.2 eV, while it is about 0.6 eV in the DFT calculation for the bulk (see. Figure S4, Supporting Information). This suggests a smaller splitting near the surface than that in the bulk, implying a significant modification of the bulk properties at the extended surface area of P-terminated $LaCo_2P_2$.

We will now discuss the previously noted kink in band 3, detected at the energy of around 40 meV. From the fact that the energy of the kink agrees with the typical phonon energies, we may assume that this kink signifies the presence of electron-phonon coupling (EPC), with the phonons most likely originating from the vibrations of light P atoms. However, keeping in mind our previously mentioned RIXS results on observation of magnons in this system,[10] we should not exclude possible contribution of magnons to the observed kink.[27,37] Upon further analysis, we will explore how electron-phonon and electron-magnon interactions affect the electronic structure.

Notice, that a closer inspection of surface state 2 also reveals a similar kink, albeit less pronounced than in band 3. To assess the strength of unveiled electron-boson coupling (EBC), we analyzed the ARPES spectral function depicted in **Figure 5**a. First, we fitted the momentum distribution curves to extract the peak positions and widths. Then, using the methodology described in refs. [38, 39], we adjusted the model parameterized bare band dispersion and Eliashberg function $\alpha^2F(\omega)$ to achieve a good agreement between the model and experimental parameters of the ARPES-derived peaks. This allowed us to determine the unperturbed electronic band and the self-energy function $\Sigma(E)$ for both bands 2 and 3.

The determined bare bands are shown as green lines in Figure 5a. From comparison with renormalized bands (red lines) it can be seen for the bulk-like band 3 the EBC is essentially stronger than for the surface state 2. The results of self-energy analysis are shown in Figure 5b–e. While for band 3 the real part of $\Sigma(E)$ reaches almost 30 meV, for the surface state 2 it is not exceeding 12 meV. Thus, EBC is stronger for bulk band 3. The energy position of the maximum in the Eliashberg function indicates that for both bands the strongest renormalization due to the EBC comes most likely from phonons with the energies of 30–40 meV.

To confirm our anticipation that the electron-phonon coupling is the origin of the kinks in bulk and surface bands seen in ARPES, we performed phonon spectrum calculations within an ab initio linear response technique.[40] The phonon dispersions, calculated along the high-symmetry directions of the bulk BZ, are shown in **Figure 6**a. The atomic localization of the modes is shown in the colors marked in the right-bottom key. As expected, the vibrations of heavy La atoms are entirely in the low-energy part of the phonon spectrum, down to 20 meV. Modes associated with displacements of Co atoms along the z direction also turn out to be low-frequency (almost dispersionless curves around 11 meV at the BZ boundary). Modes with longitudinal vibrations of Co atoms also exhibit weak dispersion. They form a bundle of four longitudinal modes around 26 meV in the upper part of the low-energy spectrum. Although these vibrations are often accompanied by twitching of P atoms along the z direction, fully z-polarized phosphorus modes lie somewhat lower in

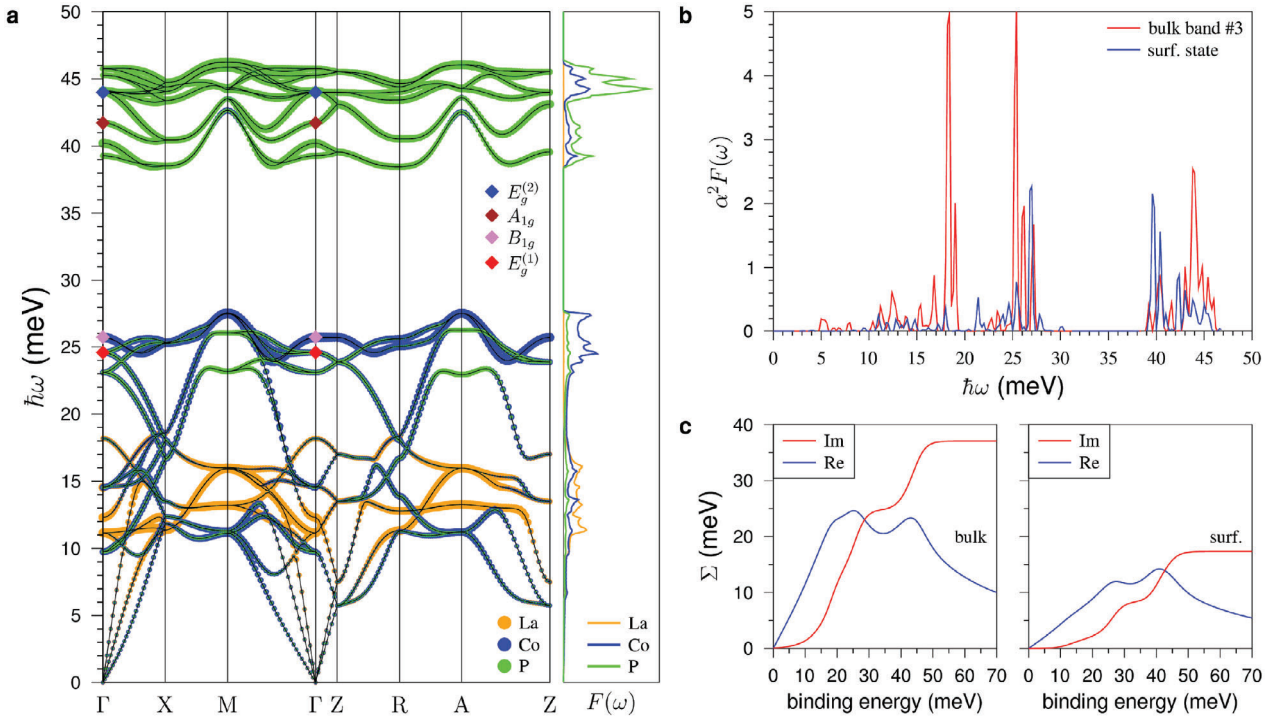

Figure 6. a) Bulk phonon spectrum (left) and corresponding partial density of states (DOSs) (right) of $LaCo_2P_2$. Orange, blue, and green circles/lines denote localization of vibration modes on La, Co, and P sublattices, respectively. b) Eliashberg functions $\alpha^2F(\omega)$ for bulk (red) and surface (blue) states just below the Fermi level. c) Re and Im parts of self-energy $\Sigma(E)$ for the band 3 (left) and surface state 2 (right) calculated for $T = 20$ K.

energy, around 24 meV. Vibrations associated with the movement of light P atoms determine the high-energy part of the spectrum with the mass difference of the atoms leading to a large energy gap (~10 meV).

In the primitive unit cell of $LaCo_2P_2$ there are four Raman active modes: $A_{1g} \bigoplus B_{1g} \bigoplus 2E_g$. The $A_{1g}(B_{1g})$ mode represents the vibrations of the P(Co) ions along the c-axis, whereas the E_g modes involve the vibration of both Co and P ions within the (001)-plane. The calculated values of Raman modes: $A_{1g} = 41.7$ meV, $B_{1g} = 25.7$ meV, and $E_g = 24.6$ and 44.0 meV (Figure 6a) agree fine with the measured Raman spectrum (see the Supporting Information, Figure S5a). The two lowest modes, $E_g^{(1)}$ and B_{1g}, contribute to peak 1 at 24.4 meV while A_{1g} and $E_g^{(2)}$ modes give rise to the peaks 2 and 3 at 40.9 and 43.1 meV, respectively. The good agreement between the experiment and theory in the description of phonons can serve as a reliable basis for calculating the electron-phonon interaction.

The strength of the EPC interaction for a particular electron state with momentum $\mathbf{k}$ and band index i, $\lambda_{\mathbf{k}_i}$, is defined using the corresponding state-dependent Eliashberg spectral function $\alpha^2F_{\mathbf{k}_i}(\omega)$:

$$\alpha^2F_{\mathbf{k}_i}(\omega) = \sum_{\mathbf{q},\nu,f} \delta(\epsilon_{\mathbf{k}+\mathbf{q}_f} - \epsilon_{\mathbf{k}_i}) \mid g^{\mathbf{q}\nu}_{\mathbf{k}+\mathbf{q}_f,\mathbf{k}_i}|^2 \delta(\omega - \omega_{\mathbf{q}\nu}). \quad (1)$$

Here the quasielastic approximation is used: $\delta(\epsilon_{\mathbf{k}+\mathbf{q}_f} - \epsilon_{\mathbf{k}_i} \mp \omega_{\mathbf{q},\nu}) \approx \delta(\epsilon_{\mathbf{k}+\mathbf{q}_f} - \epsilon_{\mathbf{k}_i})$. The sum is carried out over final electron states and all possible phonon modes ($\mathbf{q}$, ν). The spectral decomposition of the coupling constant $\lambda_{\mathbf{k}_i}$ can be obtained as

$$\lambda_{\mathbf{k}_i} = \int \{\alpha^2F_{\mathbf{k}_i}(\omega)/\omega\} d\omega. \quad (2)$$

Figure 6b shows calculated Eliashberg functions for bulk band 3 and surface state 2 where initial states lie just below the Fermi level (–0.02 eV) along the M − Γ direction. The corresponding $\lambda_{\mathbf{k}}$ constant is 1.03 for the bulk band that is in a good agreement with the value 0.85 deduced from the slope of $\mathrm{Re}\,\Sigma(E)$ (Figure 5b). It should be noted that the value of the EPC parameter only weakly depends on the choice of the initial state: for $\mathbf{k}_i$ along the M − X, the value of $\lambda_{\mathbf{k}}$ is 1.06. The calculation of the Eliashberg function for the surface state was done using the 11 ML slab. In the surface phonon spectrum all vibrational modes lie in the regions of bulk states (see the Supporting Information, Figure S6). The Eliashberg function $\alpha^2F_{\mathbf{k}_i}(\omega)$ for the surface band 2 is smaller with respect to the bulk one. This determines the electron-phonon coupling strength (0.4) being more than a factor of 2 smaller than for the bulk in agreement with ARPES observations demonstrating a weakly pronounced kink in the surface state 2.

Having the calculated Eliashberg functions for the bulk and surface bands one can get EPC contribution to the self-energy, which is accessible via ARPES measurements. The imaginary part of the quasiparticle self-energy can be expressed as

$$\mathrm{Im}\,\Sigma_{\mathbf{k}_i}(\epsilon) = -\pi \int_0^\infty d\omega \{\alpha^2F^E_{\mathbf{k}_i}(\epsilon,\omega)[b(\omega) + f(\omega+\epsilon)] + \alpha^2F^E_{\mathbf{k}_i}(\epsilon,\omega)[b(\omega) + f(\omega-\epsilon)]\}. \quad (3)$$

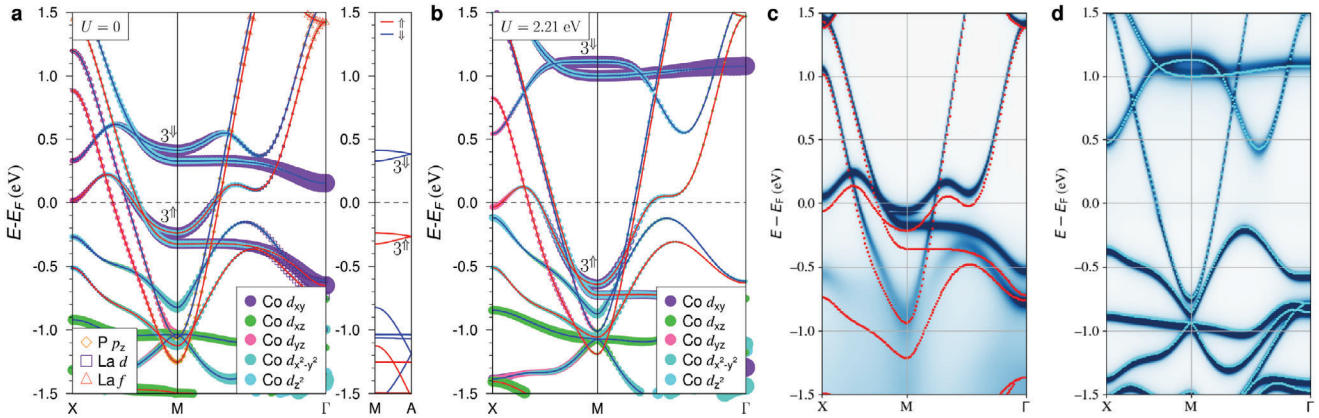

Figure 7. Bulk band structure at $U = 0$ (a) and $U = 2.21$ eV (b) calculated along high-symmetry directions of the tetragonal BZ. Red and blue lines show spin-up (⇑) and spin-down (⇓) states. Color symbols denote the weights of the orbitals pointed out in the key. Spin-up (c) and spin-down (d) quasiparticle band dispersions renormalized with the electron–magnon scattering in comparison with GGA+U band spectrum (red and light-blue for spin-up (c) and spin-down (d), respectively.

Here $b(\omega)$ and $f(\omega)$ denote Fermi and Bose distribution functions, respectively. The real part Re Σ can then be calculated from Im Σ with the help of the Kramers–Kronig relation. Figure 6c shows the calculated self-energies for the bulk (left) and surface (right) states for $T = 20$ K. Peaks in the real part occur in both cases at ≈30 − 40 meV in very good agreement with the ARPES-derived maxima in Σ (Figure 5b,d). Also the experimental peak height of Re Σ of ≈30 meV for the bulk band 3 is well matched by our calculation. At the same time, the peak height in Re Σ for the surface state is a bit larger (14 meV) compared to the fitting, but it is also much lower compared to the bulk state. Thus, our calculations support EPC origin of the kinks at E_F in both bulk and surface states. The calculation further shows that a significant part of the EPC stems from the phosphorus vibrational modes, which couple to the magnetically split Co 3d dominated states around the M point. We will now show that these states are further renormalized by electron-magnon interactions, thus suggesting an interplay between the magnetic and vibrational excitations. This is further supported by the fact that for two isostructural compounds away from the critical point of the magnetic phase transition $CeCo_2P_2$ (Co AFM order) and $EuCo_2P_2$ (Co nonmagnetic), the phosphorus vibrational modes are absent in the Raman spectra (see the Supporting Information, Figure S5b) and for $CeCo_2P_2$, no significant electron-magnon interaction was observed.[10]

Although our simplified LSDA approach allows us to capture the main spectroscopic features of the electronic structure of $LaCo_2P_2$, the correlation effects associated with the d-electrons of cobalt must definitely be taken into account, in order to describe the LSDA band structure renormalization on a greater energy scale. As a first step in improving the theoretical description of the electronic structure, we applied the DFT+U method. Co 3d states were treated using a GGA+U approach,[41,42] where the U_{eff} value was calculated using the linear response method[43] giving a value of 2.21 eV. With inclusion of U the spin magnetic moment at the Co atom in the bulk is increased to 0.657 μ_B.

With $U = 0$ our GGA calculations agree perfectly with the LSDA results presented above. As can be seen in **Figure 7a**, the band 3 observed in ARPES and the surface-projected LSDA spectrum at the $\bar{M}$ point comes from two spin-up states which are degenerate at the A point (M–A direction corresponds to the surface normal). Their spin-down counterparts lie at ≈0.4 eV above the Fermi level. These bands are mainly formed by the Co d_{xy} orbitals with sizeable contribution from Co d_{z^2}. On the whole, with exception of contributions of La d and f orbitals in the vicinity of Γ below and far above E_F, respectively, and small ones from P p_z orbitals highly dispersing parabolic bands in the M point, all bands have Co d character. The Hubbard U (Figure 7b) has relatively little impact on Co bands near the Fermi level with exception the 3⇑ and 3⇓ pairs formed by $d_{xy} + d_{z^2}$ orbitals. In particular, 3⇑ bands occur at energies from −0.7 to −0.6 eV at the M point and therefore must generate a bulk projection band at the bottom of the $\bar{M}$ gap that contradicts to the ARPES observations. Thus, one can conclude the static mean-field approach is not sufficient to describe the observed band structure and spin fluctuations should be included into consideration.

To address the effect of electron-magnon interaction on the low-energy spectrum of $LaCo_2P_2$ we performed calculations of the electronic structure taking into account bosonic spin-flip excitations via a many-body perturbation theory.[44] This approach relies on a perturbation expansion of the electronic self-energy based on the Hedin equations.[45] The electronic structure in the unperturbed state was calculated using a GGA+U functional ($U_{eff} = 2.21$ eV), which reproduces correctly spin wave spectrum and the Curie temperature in a (La,Ce)Co_2P_2.[10] Spin wave spectrum (magnons) for the tetragonal BZ is presented in **Figure 8a**. There are four magnon modes since the tetragonal unit cell contains four magnetic atoms. However, two modes are almost degenerate in the whole BZ. This indicates a weak coupling between Co magnetic moments along the z direction. Along the X-M and R-A symmetry directions the pairwise degenerate bands propagate close to each other thus showing the weakness of magnetic interaction between the magnetic moments within a Co layer in these particular directions. In the vicinity of the M point, the magnon bands are close in energy with optic phonons stemming from vibrations of phosphorous atoms (see Figure 6a). Thus, both magnons and phonons may potentially contribute to the band structure renormalization presented in Figures 4 and 5.

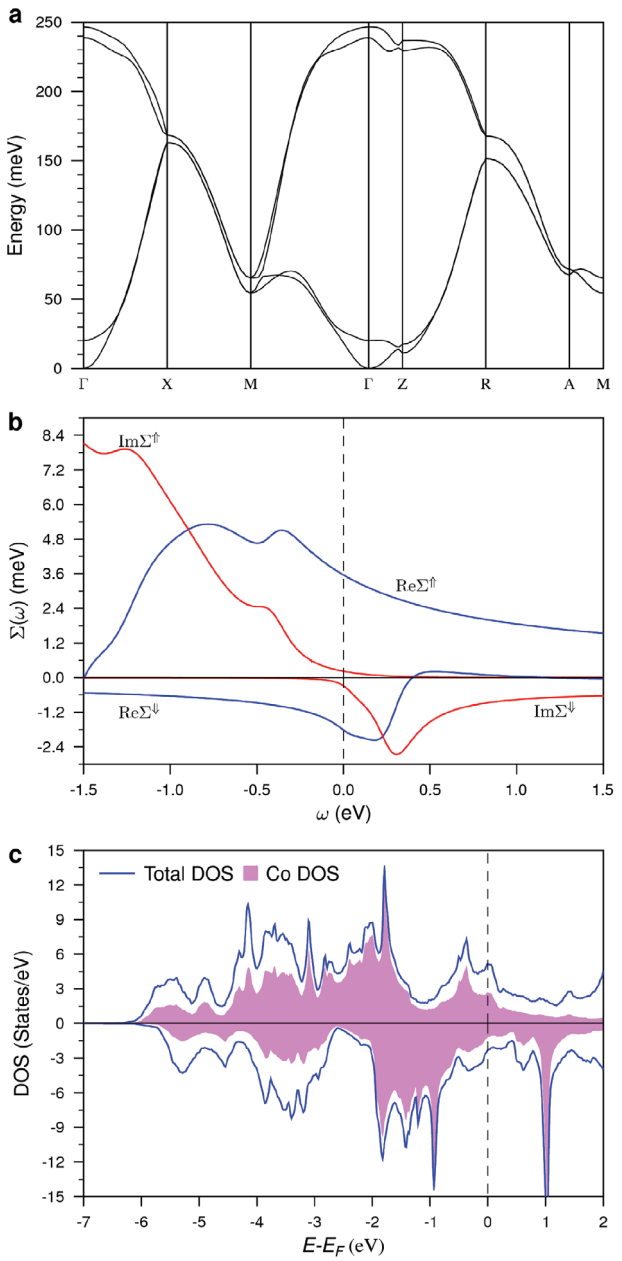

Figure 8. a) Magnon spectrum of $LaCo_2P_2$ bulk; b) Electron-magnon self energy at the Γ point and c) the spin-resolved (positive/negative for spin-up/spin-down states) total and partial Co DOS's of $LaCo_2P_2$.

The impact of the magnon scattering on the electronic structure of $LaCo_2P_2$ in the X-M-Γ direction is shown in Figure 7c,d. The most prominent changes take place in the majority spin channel (Figure 7c): the occupied bands are shifted up in energy and acquire finite life-time seen as the broadening of the spectral line. The lower energy bands shown in Figure 7c are strongly damped after the renormalization indicating pronounced electron-magnon scattering in this energy range of the corresponding electronic states. At the same time, the electronic structure in the minority spin channel (Figure 7d) is almost unaffected by the electron-magnon scattering except a very little shift in energy and non-significant broadening of the energy bands. This shift in the spin-up channel explains the results of the current ARPES experiment presented in Figure 4 and in Figure 5: the renormalized band 3 is shifted in energy towards the Fermi level and its position is now in good agreement with the ARPES experiment. However, the renormalization does not affect the shape of the band. Hence, only electron-phonon interaction is responsible for the kinks observed with ARPES.

This renormalization of the electronic structure is determined by the self-energy originating from the electron-magnon interaction: the real part of the self-energy in the majority spin channel is significantly larger then its counterpart in the minority spin channel (Figure 8b). While the spin-down self-energy is relatively small in magnitude and is practically constant in the whole energy range (except the vicinity of the Fermi level), the spin-up self-energy is of an order magnitude larger and strongly varies with the hole energy below the Fermi level. The real part of the spin-up self-energy shifts the bands in energy, while the imaginary part broadens their width. Since the imaginary part of the spin-up self-energy increases while moving down away from the Fermi level, the bands are getting broader as shown in Figure 7c. At the same time, both real and imaginary parts of the spin-up self-energy change smoothly in energy and therefore, the shape of the bands is almost not affected—they show no kinks as observed in the current experiment. Note that below the Fermi energy the majority/minority bands are renormalized toward higher/lower energies, effectively reducing the exchange splitting. This explains the overestimation of the exchange splitting within the GGA+U results discussed above. However, despite the renormalization of the spin-up bands, the Co magnetic moments are reduced from 0.61 μ_B to approximately 0.55 μ_B due to the electron-magnon interaction. The reason for this is that the electronic structure is renormalized only in some part of the BZ (see Figure S8, Supporting Information).

To understand the physics behind this spin-dependent band renormalization, we analyze the spin-resolved electron-magnon self-energy and the density of states (DOS) of $LaCo_2P_2$ (Figure 8c). The spin-up self-energy describes the decay of a majority hole into a minority hole, while the decay of a minority electron into a majority electron is given by the spin-down self-energy. During both processes, a magnon is emitted.[44] Other electron-magnon processes are weak in the strong magnets. Thus, the spin down DOS below the Fermi level reflects final states of the electron-magnon scattering in the majority spin channel, while the electron-magnon scattering in the minority spin channel is manifested by the spin-up DOS above the Fermi level. In $LaCo_2P_2$ the DOS of minority carriers below the Fermi level shows an abundance of final states while spin up DOS above the Fermi level has much fewer available final states. Thus, the significant renormalization of the band structure in the spin-up channel can be explained by the large spin-down DOS below the Fermi level in $LaCo_2P_2$. In other words, the electron-magnon self-energy in this system is dominated by the spin-dependent decay processes of the spin-up holes below the Fermi level.

3. Conclusion

In summary, the properties of the $LnCo_2P_2$ family are governed by a complex interplay of competing interactions,

leading to diverse magnetic orders both in the bulk and near their surfaces.[9,10] Unique to $LaCo_2P_2$ is the structural proximity to the critical point of the magnetic phase transition, resulting in a weak itinerant ferromagnetic order. Through careful analysis of ARPES data taken from $LaCo_2P_2$, we separated the bulk and surface electron bands. For the P-terminated surface, the Rashba effect was observed, along with the breakdown of the magnetic order of the Co 3*d* moments. In the bulk, large Co 3*d* electron pockets are found around the $\overline{M}$ point, with significantly reduced lifetimes and kinks indicating substantial electron-boson renormalization stronger than at the surface.

Our theoretical description shows that the experimentally observed electronic structure can be accurately described by DFT without inclusion of a Hubbard-term for the onsite repulsion of the Co 3*d* electrons. We find that this is a direct result of band structure renormalization due to spin excitations, which effectively suppresses the influence of the *U* term on the band structure for the majority spin channel. Furthermore, the energy-dependent reduced lifetimes and the kinks of the Co 3*d* states around the $\overline{M}$ point are attributed to phonons. Notably, vibrational modes of phosphorus, despite their minimal direct contribution to the Co 3*d* states, play a significant role.

Our results highlight how, in this weak itinerant ferromagnet, the electronic structure is strongly renormalized by electron-magnon interactions, effectively negating the strong onsite repulsion of the Co 3*d* states for the majority spin channel. Since the magnetic phase transitions in $LnCo_2P_2$ are accompanied by structural changes (see the Supporting Information, Section S1), the magnetic ground state and its excitations appear to be linked with phononic excitations. Our results suggest that the mutual interactions between electrons, phonons, and magnons are likely responsible for the unusual magnetic properties of $LaCo_2P_2$. Similar electronic states can be found in the isostructural iron pnictide superconductors, where spin excitations are believed to be essential for the emergence of superconductivity.[13] Our results also highlight the significant influence of the phonon modes on the transition metal 3*d* states, particularly the vibrational mode of the pnictogen at higher energies. It is anticipated that the $LnCo_2P_2$ series of compounds, as well as similar families containing both magnetically-active lanthanide and transition metal atoms, may serve as promising platforms for exploring complex and compelling physics both in the bulk and at the surface, driven by the Kondo and Rashba effects, exchange interactions, and electron-boson couplings.

4. Experimental Section

Sample Preparation: Single crystals of $LaCo_2P_2$ were grown from Sn flux by a modified Bridgman method in a vertical resistive furnace (GERO HTRV70250/18). Elements with an optimized initial stoichiometry of 1.6: 2: 2: 30 (La: Co: P: Sn) were placed in a graphite crucible enclosed in a welded Nb crucible. The maximum furnace temperature was ≈1400°C, and the initial heat-up rate was 100 K h^{-1} with an additional hold time of 10 h at 450°C, to ensure a complete reaction of P with Sn. A flow of argon through the growth tube was present (≈150 mL min^{-1}), which prevented oxidation of the metallic Nb crucible and provided an additional cooling at the bottom of the crucible. The tin flux was removed after growth by etching with hydrochloric acid. Further details concerning the crystal growth as well as the chemical and structural characterization can be found in ref. [29]. The growth procedure led to platelet-like samples with an area of ≈2 × 2 mm^2.

Measurement Details: Temperature-dependent ARPES experiments were performed at the BLOCH beamline of the MAX-IV laboratory.[46] The experimental station at Branchline A of BLOCH is equipped with a Scienta Omicron DA30-L analyzer, enabling high-resolution ARPES measurements. It is further equipped with a 6-axis "Carving" cryomanipulator, powered by a low-vibration, closed-cycle "Stinger" cryocooler, allowing the sample to reach a minimum temperature of 18 K. $LaCo_2P_2$ single crystals were cleaved in situ under ultra-high vacuum conditions better than 10^{-10} mbar at the lowest temperature before ARPES measurements.

DFT Calculations: Surface band structure calculations were performed with FPLO-18.00-52 code (improved version of the original FPLO code by K. Koepernik and H. Eschrig[47]). LSDA with $U = 0$ was used. The model slab consisted of 16 atomic layers. Interlayer distances were relaxed for the six outermost layers of the slab.

Phonon spectra calculations were carried out within the framework of DFT with relativistic norm-conserving pseudopotentials constructed from all-electron valence states according to the Vanderbilt scheme.[48] The exchange and correlation energy functional was described within the GGA-PBE. The lattice dynamics was studied using a linear response approach based on the DFT as implemented in the mixed-basis pseudopotential method,[49,50] which employs a combination of local functions and plane waves to represent valence states.[51] Dynamical properties were calculated using the linear response theory[40] adapted to the mixed-basis pseudopotential approach.[49]

Additional bulk electronic structure calculations were performed using Vienna Atomic Simulation Package (VASP)[52,53] within projector augmented-wave (PAW) method.[54–56] Within this approach to describe the highly correlated Co-3*d* electrons, we include the correlation effects within the GGA+*U* method[41] with *U* calculated within the linear response method.[43]

Magnetic interaction, electron-magnon coupling as well as the impact of electron-magnon interaction on the electronic structure were studied using a first-principles self-consisted Green function method implemented within the multiple scattering theory.[57,58] This method is designed for bulk, surfaces, interfaces and interfaces. The results of Green function calculations agree well with the other methods used in the current project. The self-energy of the electron-magnon coupling was calculated using a many-body perturbation theory as it is implemented within the time-dependent density functional theory and our Green function approach.[44]

Supporting Information

Supporting Information is available from the Wiley Online Library or from the author.

Acknowledgements

The authors acknowledge the German Research Foundation (DFG) for the support of our research through the grants GU2228/2-1 (Project No. 512344413), No. SFB1143 (Project No. 247310070), and TRR288 (No. 422213477, Project No. A03). The authors acknowledge Saint-Petersburg State University for a research project No. 95442847. The work of D.Y.U. and V.S.S. (analysis of the ARPES data) was supported by the Ministry of Science and Higher Education of the Russian Federation (No. 075-15-2024-632). S.P. is recipient of a DOC Fellowship of the Austrian Academy of Sciences at the Institute of mathematics, physics, space research, and materials sciences. P.A.B. and A.E. acknowledge the funding by the Österreichischer Fonds zur Förderung der Wissenschaftlichen Forschung (FWF) under Grant No. I 5384 and by the grant BU 4062/1-1 of DFG. S.V.E. acknowledge support from the Government research assignment for ISPMS SB RAS, project FWRW-2022-0001. The authors acknowledge the computing time made available to them on the high-performance computer at the NHR Center of TU Dresden. This center was jointly supported by

the Federal Ministry of Education and Research and the state governments participating in the NHR. We acknowledge MAX IV Laboratory for experimental time on BLOCH beamline under proposals 20221347 and 20211066. Research conducted at MAX IV, a Swedish national user facility, was supported by the Swedish Research Council under contract 2018-07152, the Swedish Governmental Agency for Innovation Systems under contract 2018-04969, and Formas under contract 2019-0249. The autors are particularly grateful for the expert scientific and technical support of Craig Polley and the entire BLOCH team.

Conflict of Interest

The authors declare no conflict of interest.

Author Contributions

D.V.V., C.K., and D.Y.U. designed the research. M. P., K.K, and C.K. prepared the samples for experiments. ARPES measurements were done by K.A., G.P., M.M., S.S., and D.V.V. STM studies were performed by K.B. and V.S. Raman measurements were performed by F.H. and M.R. Theoretical studies were performed by I.Y.S., E.V.V., S.P., P.A.B., R.H. A.E., S.V.E., and D.Y.U. All authors discussed the results. The manuscript was written by D.Y.U., A.E., S.V.E., and D.V.V. All authors have read and approved the decisive version of the manuscript.

Data Availability Statement

The data that support the findings of this study are available from the corresponding author upon reasonable request.

Keywords

ARPES, electron-magnon interaction, electron-phonon interaction, $LaCo_2P_2$

Received: September 18, 2024
Revised: October 10, 2024
Published online:

[1] G. R. Stewart, *Rev. Mod. Phys.* **1984**, *56*, 755.
[2] G. R. Stewart, *Rev. Mod. Phys.* **2006**, *78*, 743.
[3] F. Steglich, J. Aarts, C. D. Bredl, W. Lieke, D. Meschede, W. Franz, H. Schäfer, *Phys. Rev. Lett.* **1979**, *43*, 1892.
[4] X. Tan, Z. P. Tener, M. Shatruk, *Acc. Chem. Res.* **2018**, *51*, 230.
[5] M. Shatruk, *J. Solid State Chem.* **2019**, *272*, 198.
[6] H. Yamaoka, I. Jarrige, N. Tsujii, J.-F. Lin, T. Ikeno, Y. Isikawa, K. Nishimura, R. Higashinaka, H. Sato, N. Hiraoka, H. Ishii, K.-D. Tsuei, *Phys. Rev. Lett.* **2011**, *107*, 177203.
[7] M. Andruh, J. P. Costes, C. Diaz, S. Gao, *Inorg. Chem.* **2009**, *48*, 3342.
[8] V. Yannello, F. Guillou, A. A. Yaroslavtsev, Z. P. Tener, F. Wilhelm, A. N. Yaresko, S. L. Molodtsov, A. Scherz, A. Rogalev, M. Shatruk, *Chem. Eur. J.* **2019**, *25*, 5865.
[9] G. Poelchen, I. P. Rusinov, S. Schulz, M. Güttler, M. Mende, A. Generalov, D. Y. Usachov, S. Danzenbächer, J. Hellwig, M. Peters, K. Kliemt, Y. Kucherenko, V. N. Antonov, C. Laubschat, E. V. Chulkov, A. Ernst, K. Kummer, C. Krellner, D. V. Vyalikh, *ACS Nano* **2022**, *16*, 3573.
[10] G. Poelchen, J. Hellwig, M. Peters, D. Y. Usachov, K. Kliemt, C. Laubschat, P. M. Echenique, E. V. Chulkov, C. Krellner, S. S. P. Parkin, D. V. Vyalikh, A. Ernst, K. Kummer, *Nat. Commun.* **2023**, *14*, 5422.
[11] M. Reehuis, W. Jeitschko, *J. Phys. Chem. Solids* **1990**, *51*, 961.
[12] M. Rotter, M. Tegel, D. Johrendt, *Phys. Rev. Lett.* **2008**, *101*, 107006.
[13] R. M. Fernandes, A. Coldea, H. Ding, I. R. Fisher, P. J. Hirschfeld, G. Kotliar, *Nature* **2022**, *601*, 35.
[14] T. Mine, H. Yanagi, T. Kamiya, Y. Kamihara, M. Hirano, H. Hosono, *Solid State Commun.* **2008**, *147*, 111.
[15] F. Ronning, N. Kurita, E. D. Bauer, B. L. Scott, T. Park, T. Klimczuk, R. Movshovich, J. D. Thompson, *J. Phys.: Condens. Matter* **2008**, *20*, 342203.
[16] C. Meingast, A. Shukla, L. Wang, R. Heid, F. Hardy, M. Frachet, K. Willa, T. Lacmann, M. Le Tacon, M. Merz, A.-A. Haghighirad, T. Wolf, *Phys. Rev. B* **2022**, *106*, 144507.
[17] W. Jeitschko, R. Glaum, L. Boonk, *J. Solid State Chem.* **1987**, *69*, 93.
[18] Q. Guo, B.-J. Pan, J. Yu, B.-B. Ruan, D.-Y. Chen, X.-C. Wang, Q.-G. Mu, G.-F. Chen, Z.-A. Ren, *Sci. Bull.* **2016**, *61*, 921.
[19] N. Berry, C. Capan, G. Seyfarth, A. D. Bianchi, J. Ziller, Z. Fisk, *Phys. Rev. B* **2009**, *79*, 180502.
[20] A. Pandey, D. G. Quirinale, W. Jayasekara, A. Sapkota, M. G. Kim, R. S. Dhaka, Y. Lee, T. W. Heitmann, P. W. Stephens, V. Ogloblichev, A. Kreyssig, R. J. McQueeney, A. I. Goldman, A. Kaminski, B. N. Harmon, Y. Furukawa, D. C. Johnston, *Phys. Rev. B* **2013**, *88*, 014526.
[21] N. Xu, P. Richard, A. van Roekeghem, P. Zhang, H. Miao, W.-L. Zhang, T. Qian, M. Ferrero, A. S. Sefat, S. Biermann, H. Ding, *Phys. Rev. X* **2013**, *3*, 011006.
[22] D. Kasinathan, A. Ormeci, K. Koch, U. Burkhardt, W. Schnelle, A. Leithe-Jasper, H. Rosner, *New J. Phys.* **2009**, *11*, 025023.
[23] P. D. C. King, S. Picozzi, R. G. Egdell, G. Panaccione, *Chem. Rev.* **2021**, *121*, 2816.
[24] A. Chikina, M. Höppner, S. Seiro, K. Kummer, S. Danzenbächer, S. Patil, A. Generalov, M. Güttler, Y. Kucherenko, E. V. Chulkov, Y. M. Koroteev, K. Koepernik, C. Geibel, M. Shi, M. Radovic, C. Laubschat, D. V. Vyalikh, *Nat. Commun.* **2014**, *5*, 3171.
[25] M. Güttler, A. Generalov, M. M. Otrokov, K. Kummer, K. Kliemt, A. Fedorov, A. Chikina, S. Danzenbächer, S. Schulz, E. V. Chulkov, Y. M. Koroteev, N. Caroca-Canales, M. Shi, M. Radovic, C. Geibel, C. Laubschat, P. Dudin, T. K. Kim, M. Hoesch, C. Krellner, D. V. Vyalikh, *Sci. Rep.* **2016**, *6*, 24254.
[26] A. Generalov, M. M. Otrokov, A. Chikina, K. Kliemt, K. Kummer, M. Höppner, M. Güttler, S. Seiro, A. Fedorov, S. Schulz, S. Danzenbächer, E. V. Chulkov, C. Geibel, C. Laubschat, P. Dudin, M. Hoesch, T. Kim, M. Radovic, M. Shi, N. C. Plumb, C. Krellner, D. V. Vyalikh, *Nano Lett.* **2017**, *17*, 811.
[27] F. Mazzola, C.-M. Yim, V. Sunko, S. Khim, P. Kushwaha, O. J. Clark, L. Bawden, I. Marković, D. Chakraborti, T. K. Kim, M. Hoesch, A. P. Mackenzie, W. P., P. D. C. King, *npj Quantum Mater.* **2022**, *7*, 20.
[28] A. V. Tarasov, M. Mende, K. Ali, G. Poelchen, S. Schulz, O. Y. Vilkov, K. A. Bokai, M. Muntwiler, V. Mandic, C. Laubschat, K. Kliemt, C. Krellner, D. V. Vyalikh, D. Y. Usachov, *Surf. Interfaces* **2022**, *32*, 102126.
[29] K. Kliemt, M. Peters, F. Feldmann, A. Kraiker, D.-M. Tran, S. Rongstock, J. Hellwig, S. Witt, M. Bolte, C. Krellner, *Cryst. Res. Technol.* **2019**, *55*, 1900116.
[30] M. Reehuis, C. Ritter, R. Ballou, W. Jeitschko, *J. Magn. Magn. Mater.* **1994**, *138*, 85.
[31] A. Aguayo, I. I. Mazin, D. J. Singh, *Phys. Rev. Lett.* **2004**, *92*, 147201.
[32] O. Krupin, G. Bihlmayer, K. M. Döbrich, J. E. Prieto, K. Starke, S. Gorovikov, S. Blügel, S. Kevan, G. Kaindl, *New J. Phys.* **2009**, *11*, 013035.
[33] S. Schulz, I. A. Nechaev, M. Güttler, G. Poelchen, A. Generalov, S. Danzenbächer, A. Chikina, S. Seiro, K. Kliemt, A. Y. Vyazovskaya, T. K. Kim, P. Dudin, E. V. Chulkov, C. Laubschat, E. E. Krasovskii, C. Geibel, C. Krellner, K. Kummer, D. V. Vyalikh, *npj Quantum Mater.* **2019**, *4*, 26.
[34] D. Y. Usachov, M. Güttler, S. Schulz, G. Poelchen, S. Seiro, K. Kliemt, K. Kummer, C. Krellner, C. Laubschat, E. V. Chulkov, D. V. Vyalikh, *Phys. Rev. B* **2020**, *101*, 245140.

[35] G. Bihlmayer, P. Noël, D. Vyalikh, E. V. Chulkov, A. Manchon, *Nat. Rev. Phys.* **2022**, *4*, 642.
[36] B. L. Gyorffy, A. J. Pindor, J. Staunton, G. M. Stocks, H. Winter, *J. Phys. F: Metal Phys.* **1985**, *15*, 1337.
[37] E. Młyńczak, M. C. T. D. Müller, P. Gospodarič, T. Heider, I. Aguilera, G. Bihlmayer, M. Gehlmann, M. Jugovac, G. Zamborlini, C. Tusche, S. Suga, V. Feyer, L. Plucinski, C. Friedrich, S. Blügel, C. M. Schneider, *Nat. Commun.* **2019**, *10*, 505.
[38] A. Fedorov, N. Verbitskiy, D. Haberer, C. Struzzi, L. Petaccia, D. Usachov, O. Vilkov, D. Vyalikh, J. Fink, M. Knupfer, B. Büchner, A. Grüneis, *Nat. Commun.* **2014**, *5*, 3257.
[39] D. Y. Usachov, A. V. Fedorov, O. Y. Vilkov, I. I. Ogorodnikov, M. V. Kuznetsov, A. Grüneis, C. Laubschat, D. V. Vyalikh, *Phys. Rev. B* **2018**, *97*, 085132.
[40] S. Baroni, S. de Gironcoli, A. Dal Corso, P. Giannozzi, *Rev. Mod. Phys.* **2001**, *73*, 515.
[41] V. I. Anisimov, J. Zaanen, O. K. Andersen, *Phys. Rev. B* **1991**, *44*, 943.
[42] S. Dudarev, G. Botton, S. Savrasov, C. Humphreys, A. Sutton, *Phys. Rev. B* **1998**, *57*, 1505.
[43] M. Cococcioni, S. de Gironcoli, *Phys. Rev. B* **2005**, *71*, 035105.
[44] S. Paischer, G. Vignale, M. I. Katsnelson, A. Ernst, P. A. Buczek, *Phys. Rev. B* **2023**, *107*, 134410.
[45] L. Hedin, *Phys. Rev.* **1965**, *139*, A796.
[46] C. M. Polley, M. Leandersson, J. Adell, J. Osiecki, D. Carbone, K. Ali, H. Fdderwitz, T. Balasubramanian, *Synchrotron Radiation News* **2024**.
[47] K. Koepernik, H. Eschrig, *Phys. Rev. B* **1999**, *59*, 1743.
[48] D. Vanderbilt, *Phys. Rev. B* **1985**, *32*, 8412.
[49] R. Heid, K. P. Bohnen, *Phys. Rev. B* **1999**, *60*, R3709.
[50] B. Meyer, C. Elsässer, F. Lechermann, M. Fähnle, *FORTRAN90 Program for Mixed-Basis Pseudopotential Calculations for Crystals, Max-Planck-Institut für Metallforschung, Stuttgart (unpublished)*.
[51] S. G. Louie, K.-M. Ho, M. L. Cohen, *Phys. Rev. B* **1979**, *19*, 1774.
[52] G. Kresse, J. Furthmüller, *Phys. Rev. B* **1996**, *54*, 11169.
[53] G. Kresse, D. Joubert, *Phys. Rev. B* **1999**, *59*, 1758.
[54] P. E. Blöchl, O. Jepsen, O. K. Andersen, *Phys. Rev. B* **1994**, *49*, 16223.
[55] P. E. Blöchl, *Phys. Rev. B* **1994**, *50*, 17953.
[56] G. Kresse, D. Joubert, *Phys. Rev. B* **1999**, *59*, 1758.
[57] M. Geilhufe, S. Achilles, M. A. Köbis, M. Arnold, I. Mertig, W. Hergert, A. Ernst, *J. Phys.: Condens. Matter* **2015**, *27*, 435202.
[58] M. Hoffmann, A. Ernst, W. Hergert, V. N. Antonov, W. A. Adeagbo, M. R. Geilhufe, H. Ben Hamed, *Phys. Status Solidi B* **2020**, *257*, 1900671.